Universal scaling laws in nanoplasmonics of laser-ionized nanospheres

V. Leshchenko,[1,2,*] A. Camacho Garibay,[1] B. Smith,[1] P. Agostini,[1] and L. F. DiMauro[1]
[1]*Department of Physics, The Ohio State University, Columbus, Ohio 43210, USA*
[2]*NeXUS facility, Institute for Optical Science, The Ohio State University, Columbus, Ohio 43210, USA*

(Received 9 March 2024; accepted 2 July 2024; published 18 July 2024)

Over the last decade, strong-field nanoplasmonics has emerged as a field for which subwavelength localization of light plays a crucial role. We present universal scaling laws for ion cutoff and anisotropy in laser-nanosphere ionization and experimentally demonstrate that the wavelength dependence of the local nanoscale field enhancement can be deduced by measuring the ion anisotropy. The results open new directions in studies of nanotargets by detecting angular-dependent charge particle distribution.

DOI: 10.1103/PhysRevA.110.013117

I. INTRODUCTION

Nanostructures have fundamental importance to a broad range of phenomena in nature as they display characteristics between isolated atoms and condensed matter systems, giving rise to unique phenomena [1,2]. In the context of strong-field physics, nanostructures are important due to their capability to enhance electric fields in well-defined spaces much smaller than the optical wavelength of the driving laser [3]. While future applications trend to complex shapes, like nanoneedles or nanoantennae [3], nanospheres remain as important fundamental targets for basic research. They can be produced in a controlled way with relative ease, and their symmetry facilitates interpretation. The promise of novel developments, such as realizing ultrafast light-wave driven nanelectronics, continue propelling fundamental research of the interaction between strong lasers and nanometric systems [2]. In addition to fundamental studies, there are a broad range of applications [4,5], which would profit from a comprehensive description of laser-induced polarization and ionization of nanoparticles and nanoclusters in a form that can be directly used for the development of, e.g., sensors. Previous fundamental studies summarized in the following few paragraphs were mostly focused on the investigation of one nanocluster property or parameter. Therefore, we derive universal scaling laws for ion cutoff and anisotropy that enable the development of novel techniques to measure nanocluster size, permittivity, and polarizability.

A plethora of different spherical nanotargets have been investigated during the past decades, including dielectric [3,6], metallic [2,3,6,7], and noble-gas nanoclusters [2,6,8], providing valuable fundamental insight as well as promising applications. For example, they can be used for the generation of high-energy electrons [2,3,7], multiply charged ions [2], as well as high-frequency photons [9,10]. Many results observed in rare gases were successfully interpreted through ionization theories based on the nanoplasma model [8,11,12]. As current experimental capabilities allow us to move away from popular 0.8 μm pulses and explore longer wavelengths, this model appears to be insufficient to describe the interaction [13,14]. Thus, extending strong-field nanophotonics and nanoplasmonics into the middle-infrared (mid-IR) spectral range is fundamental to further our understanding and guide technological developments.

Here, we study strong-field interactions of argon nanoclusters with intense ultrashort optical pulses encompasing the visible (VIS), near-infrared (NIR), and mid-IR spectral ranges. The fundamental importance of the local field enhancement is experimentally confirmed in the measured wavelength dependence of angular-resolved ion emission from laser ionized argon nanoclusters. In addition, we derive universal scaling laws for ion anisotropy and energy cutoff that are in perfect agreement with the results of both experiments and molecular dynamics (MD) simulations.

The objective of this work is to reveal the nature of two distinctive features of the ion distribution from laser-ionized nanospheres. The scaling of the ion energy cutoff and anisotropy as a function of cluster and laser parameters are presented in Secs. III and IV, respectively. Although these two characteristics are extracted from the same data set, they show distinctively different scaling with laser and cluster parameters. The nature of this difference is discussed in Sec. V.

II. EXPERIMENTAL SETUP

Our home-built Ti:Sapphire laser system, providing 0.8 μm wavelength pulses with 60-fs pulse duration and 5.6-mJ energy at 1-kHz repetition rate, is used to drive the experiment shown schematically in Fig. 1. Linearly polarized optical pulses with >1 μm wavelengths are generated with an optical parametric amplifier (OPA) (HE-TOPAS, Light Conversion), while those <0.8 μm are obtained as the second harmonic of OPA or Ti:Sapphire pulses generated in a beta barium borate (BBO) crystal. Argon van der Waals nanoclusters are obtained through a solenoid-driven (Even-Lavie [15]) pulsed gas

*Contact author: vyacheslav.leshchenko.1@gmail.com; Present address: Linac Coherent Light Source, SLAC National Accelerator Laboratory, Menlo Park 94025, California, USA.

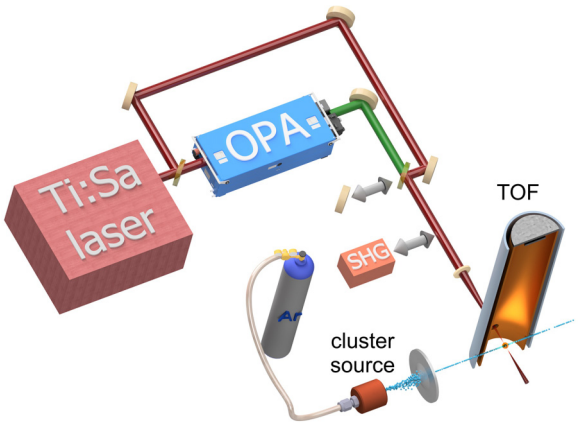

FIG. 1. Scheme of the experimental setup. The broad range of wavelengths of the optical pulse is enabled by using OPA, the direct output of the Ti:Sapphire laser, and their second harmonic. Nanoclusters are generated with a pulsed nozzle and skimmed before entering the interaction zone where they are ionized by the optical pulse, and the kinetic energy of the generated ions is detected with a TOF spectrometer.

nozzle with 150 μm diameter whose size is controlled via valve backing pressures up to 30 bar. The cluster jet is skimmed before entering the interaction region where, after exposure to the laser, the emitted ions and their kinetic energies are detected in a time-of-flight (TOF) spectrometer. Note that clusters with radius larger than 2 nm, as in our experiments, have a shape very close to spherical [16,17]. The interested reader can find additional details on the experimental setup in a previous publication [14]. Note that we do not discriminate ion charge states in the standard configuration of the setup; thus, most of the data presented here are for ion kinetic energy integrated over all ion states.

Figure 2 shows a typical ion energy spectra, where the blue curve represents ions emitted along the laser polarization, while the orange one corresponds to those emitted in an orthogonal direction. Throughout the paper, we define the anisotropy as the ratio of the mean energies of ions emitted along and orthogonal to the laser polarization

$$A = \frac{\langle K \rangle_{\parallel}}{\langle K \rangle_{\perp}}, \tag{1}$$

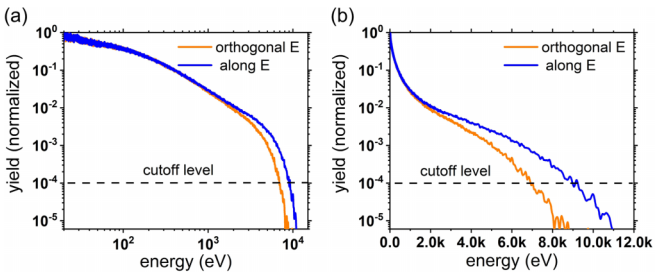

FIG. 2. Typical measured ion spectra. Both (a) and (b) are measured with 1.3 μm optical pulse of 50 fs pulse duration and 900 TW/cm^2 intensity. (a) has logarithmic energy scale, while (b) has a liner scale. Otherwise, (a) and (b) present the same results. The blue (orange) curves correspond to results measured along (orthogonal to) the laser polarization.

where K is the ion kinetic energy. The mean energy is defined as $\langle K \rangle = \int KY(K)dK / \int Y(K)dK$, where Y is the measured ion yield, e.g., in Fig. 2. In the following discussion the ion energy cutoff is defined as the kinetic energy at which the normalized yield (see Fig. 2) is crossing the 10^{-4} level. It corresponds to the threshold beyond which the ion yield quickly drops.

III. ION CUTOFF SCALING

Over the last few decades, the duration and intensity of the optical pulse were shown to impact the electron kinetic energy and x-ray yield in the laser-nano-sphere ionization [18,19]. The influence of intensity is usually attributed to inverse Bremsstrahlung (IBS) [11], an essential process to explain the enhanced absorption for longer pulses where the system can reach the plasma resonance condition [20]. In addition, larger nanotarget size increases both the mean and cutoff energy of the emitted electrons and ions [21,22]. Although most experiments (which were performed at 0.8 μm) are consistent with calculations based on the nanoplasma model [11], recent measurements of electron emission at longer wavelengths display clear deviations associated with subcycle strong-field dynamics that provides a universal scaling law of their cutoff [22]. However, a systematic discussion of a unified scaling law of ion kinetic energy, especially as a function of wavelength, is still missing. In the following, we present a systematic scan of different laser and cluster parameters and derive an expression describing a unified scaling law of the ion cutoff in laser-ionized cluster expansion.

Figure 3(a) presents our experimental results on the dependence of the ion energy on the pulse intensity and wavelength, for a fixed pulse duration (50 ± 10 fs) and 7-nm average cluster radius. As demonstrated in Fig. 3(b) all plots follow the same trend when it is rescaled to the dependence on (intensity $\times$ number of optical cycles in the pulse). This result is in perfect agreement with IBS plasma heating. The IBS heating rate is given by [11]

$$\frac{\partial U}{\partial t} = \frac{9\omega}{8\pi} \frac{\mathrm{Im}[\varepsilon]}{|\varepsilon + 2|^2} |E(t)|^2, \tag{2}$$

where U is the cycle-averaged energy absorbed by the nanoplasma, E_0 is the electric field amplitude of the pulse, and ε the permittivity of the plasma. The electric permittivity of the system can be calculated using the Drude approximation as follows:

$$\varepsilon = 1 - \frac{\omega_p^2}{\omega(\omega + i\nu)}, \tag{3}$$

where $\omega_p = \sqrt{4\pi n}$ is the plasma frequency (in atomic units), ν the collision frequency between electrons and ions in the plasma, and n is the plasma density. The universal scaling is understood when Eq. (2) is integrated and expressed as

$$U = \frac{9}{4} |E_0|^2 \int_{-\infty}^{\infty} \frac{\mathrm{Im}[\varepsilon]}{|\varepsilon + 2|^2} f(N)\, dN, \tag{4}$$

implying that the total absorbed energy is proportional to the number of cycles, provided that the term $\mathrm{Im}[\varepsilon]/|\varepsilon + 2|^2$ does not overall depend strongly on the pulse frequency [here we explicitly introduce the pulse envelope as the function of the

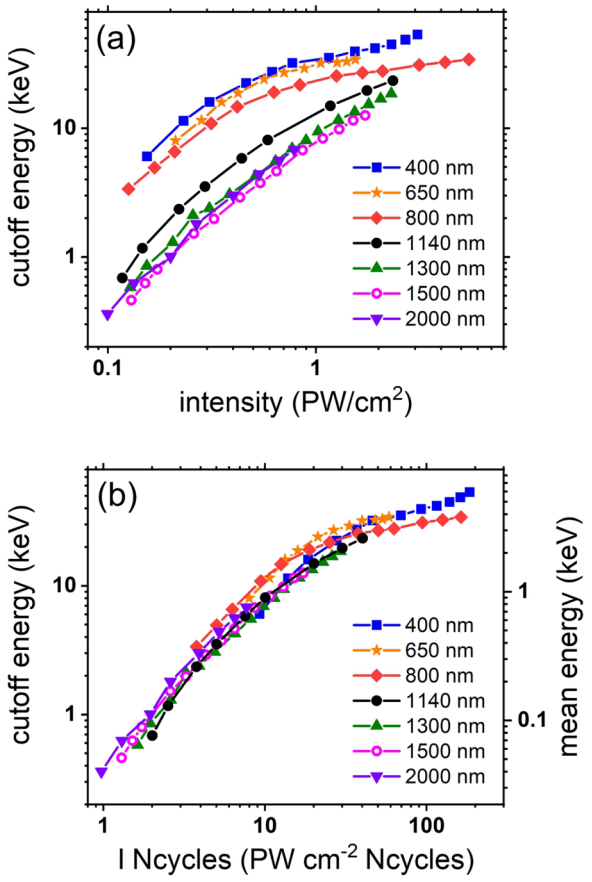

FIG. 3. (a) Measured dependence of the ion cutoff on intensity and wavelength of optical pulses. For all wavelengths, the pulse duration is about 50 fs. The averaged cluster radius is measured to be 7 nm. (b) Same, but the X scale is normalized to intensity divided by wavelength (more precisely, it is the product of intensity and the number of optical cycles (N_{cycles}) in the pulse duration, where the slight difference in the pulse duration for different wavelengths is taken into account).

number of optical cycles $f(N_{\text{cycles}})$]. In the context of the nanoplasma model, this constraint implies that the collisional frequency has to obey the relation $\nu \propto \frac{n}{\omega}$ very closely for a wide range of wavelengths (see Appendix A for more details).

It should be noted that the cutoff slope is not linear with intensity, as one may expect from Eqs. (2) and (4). This responds to the fact that the deposited energy is converted not only into plasma heating, but also into further collisional ionization (as evidenced by higher ionic charge states at higher intensity, as can be seen in Appendix B). The ionization potential for increasingly charged ions grows almost linearly for electrons located in the valence shell, but further ionization ($q > 8$) shows a pronounced jump in the required energy, tampering with the way energy is distributed among these channels. Note also that the shape of the ion spectra does not have any significant dependence on either laser intensity or wavelength, and the ratio between ion cutoff and ion mean energy stay constant, as reflected in the right scale in Fig. 3(b).

We continue our study with a less explored parameter, namely, the laser pulse duration. Measured and simulated dependence of the ion cutoff on the pulse duration and fluence

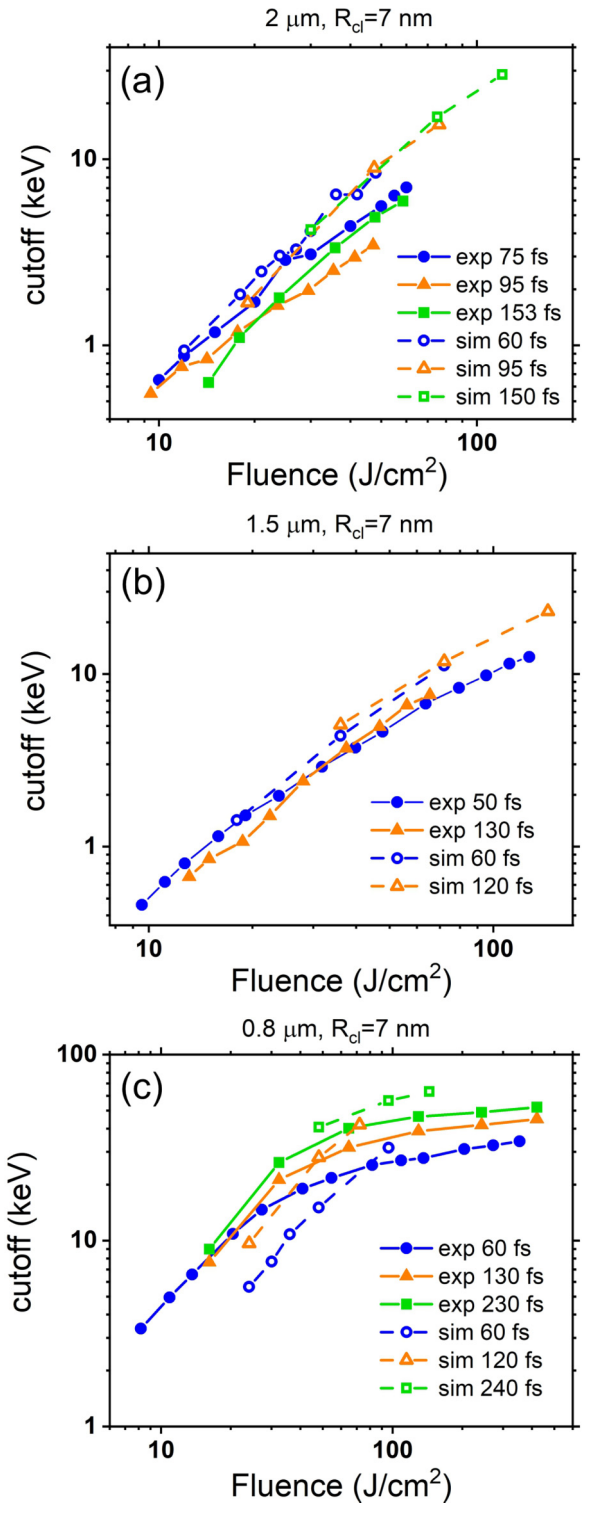

FIG. 4. Dependence of the cutoff on the pulse duration and fluence for (a) 2 μm, (b) 1.5 μm, and (c) 0.8 μm."sim" indicates MD-simulation results; "exp" stands for experimental results.

is presented in Fig. 4. The results demonstrate that the ion cutoff indeed scales according to the product of intensity and pulse duration, i.e., the fluence, as expected from Eq. (2). However, the results for 800 nm also indicate that deviations from that scaling do occur. These are caused by intrapulse resonances mentioned in previous works [21], when the plasma

has enough time to expand within the laser pulse duration to reach critical density and cause enhanced resonant absorption at the tail of the pulse. It is a similar effect to resonances in double pulse ionization discussed in our previous paper [14], further supported by the shared feature between spectra for longer pulses and for resonance conditions in the double pulse experiment (see Appendix C for more details).

The absolute value of the ion cutoff energy can be compared with estimates based on the cluster Coulomb explosion model [23] even though it is derived for a two orders of magnitude higher laser intensity. In the optical intensity regime relevant to our experiments, the build up of the positive net charge in a nanoplasma is caused by the escape of the fastest portion of electrons with enough kinetic energy to overcome the potential barrier of the nanoplasma (it is the so-called electron outerionization discussed, e.g., in our previous paper [14]). For example, in the performed MD simulations at 800 nm, 60 fs, 0.7 PW/cm^2, the total net charge of the nanoplasma at the end of the optical pulse is $Q = +3800$ e, which corresponds to 8-keV ion kinetic energy in a simple Coulomb explosion model: QZe^2/r (Z is the maximum ion charge state, which is 10 in the discussed conditions as presented in Appendix D; r is the cluster radius) [23]. The estimate is in reasonable agreement with the experimental and MD-simulations results, which have almost a factor of 3 higher cutoff that is caused by neglecting plasma hydrodynamic pressure and inhomogeneous charge distribution in a simplified Coulomb explosion model [23].

The cluster size is a parameter that was found to be important in our experiments, yet absent in Eq. (2). The cluster size is experimentally controlled by the backing pressure of the gas jet and measured via Rayleigh scattering and interferometry [14,24] (see Appendix in [14] for more details). A linear trend of the increased cutoff with the cluster size is easily identifiable in our experimental results presented in Fig. 5. Note that the average ion charge state also has linear dependence on the cluster size [see Fig. 11(a)], and the scaling of the cutoff with the cluster size follows the increase of the averaged ion charge state [see Fig. 11(b)]. This dependence is in full agreement with the expected scaling of the ion kinetic energy in a thermalized plasma at the end of its expansion [25]

$$K_{\text{ions}} = (Z+1)kT_e, \tag{5}$$

where Z is the ion charge; T_e is the electron temperature. The plasma electron temperature has almost no dependence on the cluster size, as shown in previous publications [22].

In summary, the kinetic energy of ions from the expansion of nanoplasmas created by laser ionized nanoclusters scales according to the following relation:

$$K_{\text{ions}}^{\text{cutoff}} \propto f(I)\tau R_{\text{cl}}/\lambda, \tag{6}$$

where I, λ, and τ are the laser intensity, wavelength, and pulse duration, respectively; R_{cl} is the radius of the nanosphere. $f(I)$ is a function describing the unified intensity dependence, which approximately scales as

$$f(x) \approx \begin{cases} 1.2x^{0.9} - 1, \text{ for } x < 20\,\text{PW/cm}^2 \times N_{\text{cycles}} \\ 8.5x^{0.33} - 5, \text{ for } x > 20\ \text{PW/cm}^2 \times N_{\text{cycles}}, \end{cases} \tag{7}$$

where $x = I \times N_{\text{cycles}}$.

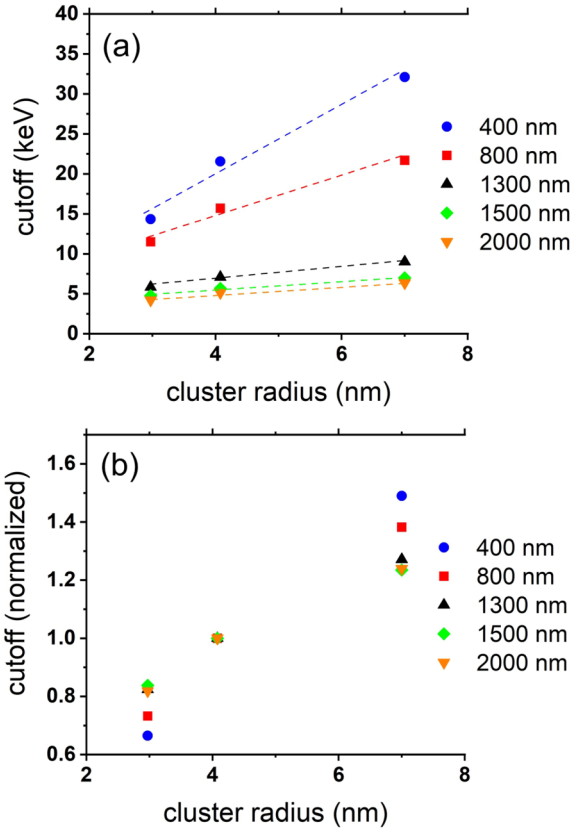

FIG. 5. (a) Measured dependence of the ion cutoff on the cluster size. Dashed lines are linear fits to the data of the same color. All results are taken at the same intensity (within about 5% absolute accuracy) of 800 TW/cm^2 and identical pulse duration of 50 ± 10 fs. (b) Same as (a) but the cutoff is normalized to the value at 4-nm cluster radius.

IV. ION ANISOTROPY SCALING

The anisotropy of the ion kinetic energy distribution has distinctively different dependence on experimental parameters compared to the cutoff, as discussed in this section. In particular, we identified that anisotropy has a much more direct correspondence to the local field enhancement in nanostructures, making the results relevant to a broad range of nanophotonics and nanoplasmonics phenomena.

Previous studies on ionic emission anisotropy were limited to a small parameter range [13,26,27], restricting the understanding, interpretation, and theoretical description of the phenomenon. Just recently a thorough study with varying pulse wavelength was performed [13] and provided new insight. We present here a thorough analysis of ionic emission anisotropy and its theoretical interpretation by scanning over an even larger parameter space. Our conclusions, therefore, are supported by a uniquely large set of experiments with varying pulse wavelength, intensity, pulse duration, and target size.

The measured dependence of ion anisotropy with respect to wavelength and intensity of the optical pulse is presented in Fig. 6. At first glance, no obvious scaling can be identified in Fig. 6(a). However, the previously observed [13] rescaling of $I \times \lambda$ reveals a universal scaling as shown in Fig. 6(b). Our interpretation of the experimental results is supported by MD

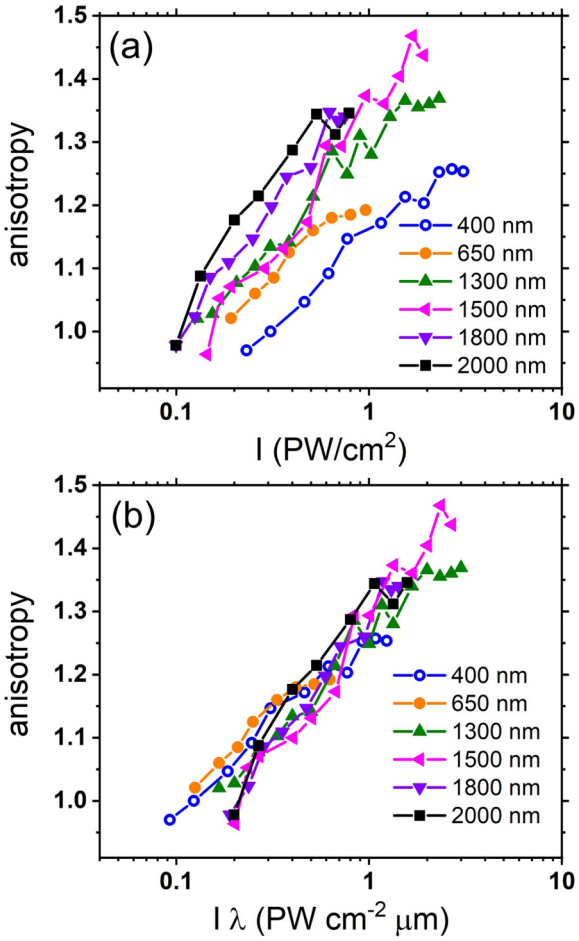

FIG. 6. (a) The measured dependence of the ion anisotropy on intensity and wavelength of optical pulses. For all wavelengths, the pulse duration is about 50 fs. The averaged cluster radius is measured to be 7 nm. (b) Same as (a), but the X scale is normalized to intensity times wavelength.

simulations, and both are presented side-by-side in Fig. 7. Note that the anisotropy in simulations is evaluated using the same approach as in experiments. Like measurements, simulation results collapse into a single line when scaled according to the $I \times \lambda$. The slightly higher slope observed in the simulation is due to the absence of focal volume averaging caused by the need to reduce computational costs. Including full focal averaging in simulations will inevitably lead to a better agreement [13].

The next parameter, which was important for the cutoff scaling, is the pulse duration. Anisotropy is largely unaffected by the pulse duration and only depends on the pulse intensity as shown in more detail in Appendix B (Fig. 12). At first glance, these results seem to contradict previously reported data [26] regarding the ion anisotropy dependence on the pulse duration. However, those results were obtained by maintaining an approximately fixed pulse energy, such that shorter pulses imply higher pulse intensities. Therefore, there is a general agreement between both results as the measured trend in that study is determined by the intensity drop for stretched pulses and consistent with our observations for pulses longer than 30 fs.

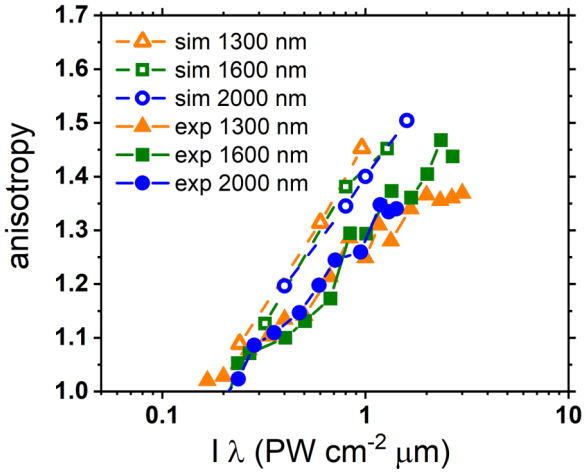

FIG. 7. Comparison of ion anisotropy in experiments and MD simulations. "sim" stands for simulations; "exp" stands for experimental results.

The nanocluster radius was another parameter important for the ion cutoff. The experimental results of the cluster size scan are shown in Fig. 8. The systematic trend of increasing anisotropy for larger nanospheres agrees with previous results [26]. However, the dependence is very week, so that doubling

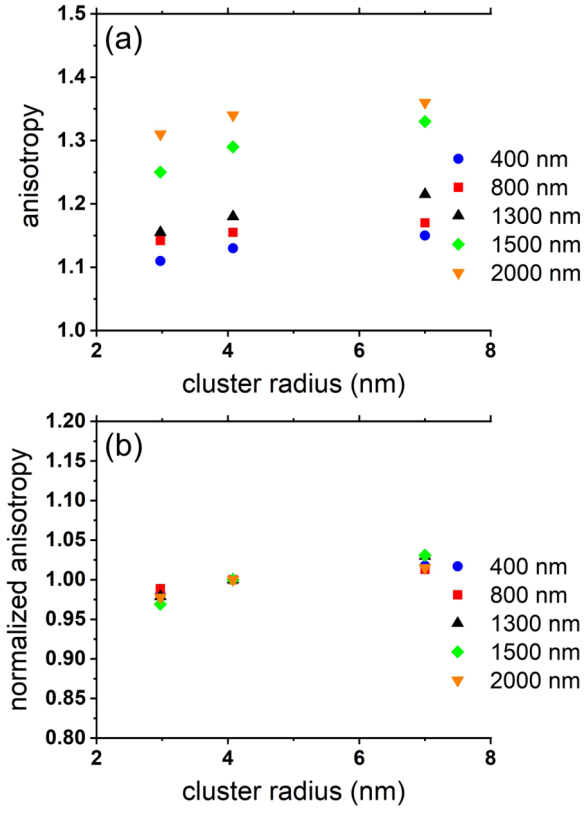

FIG. 8. (a) Measured dependence of the ion kinetic energy anisotropy on the cluster size. All results are taken at the same intensity (within about 5% absolute accuracy) of 800 TW/cm^2 and identical pulse duration of 50 ± 10 fs. (b) Same as (a) but the anisotropy is normalized to the value at the cluster radius of 4 nm.

the cluster size results in just a few-percent-increase of the ion anisotropy. Thus, ion anisotropy has negligible dependence on the nanocluster size, at least in the parameter range accessible in our experimental setup.

In summary, the anisotropy in the kinetic energy of ions from laser-ionized nanoclusters scales according to the following relation:

$$A \propto I\lambda, \tag{8}$$

while the cluster size and pulse duration have no discernible effect.

V. DISCUSSION

Our results show that the anisotropy and cutof energy have quite different scaling [see Eqs. (6) and (8)], the first shows a proportionality with the wavelength and the second with the laser frequency. Moreover, cutoff has a clear dependence on the pulse duration (and more generally the number of cycles) and the cluster size, unlike the anisotropy. These differences are clear indicators of a very different physical origin of the cutoff and anisotropy, therefore providing a glimpse into different parameters of the nanostructure, important for the characterization and development of applications.

Specifically, the measured cutoff scaling is appropriately described by the well-known process of inverse Bremsstrahlung heating [Eq. (4)], which is in agreement with previously published results [11,21,28]. Ion anisotropy, however, was previously attributed to different mechanisms such as polarization enhanced ionization or "charge flipping" [26,29,30], based on assumptions involving inhomogeneous forces arising in a homogeneous system. Recently, the basics of the inhomogeneous system charging were resolved by experiments with tunable wavelength [13]. However, a complete understanding requires to address the anisotropy dependence on other laser parameters, which has not been done previously.

As mentioned earlier, local field enhancement plays an important role in nanophotonics and nanoplasmonics, as ionization is initially driven by strong-field ionization effects that are highly sensitive to the laser field. The electric field at the surface of a sphere with size smaller than the wavelength of the incident field (which is perfectly satisfied in our experiments) can be described within Rayleigh's quasistatic dipole approximation [31,32]

$$\mathbf{E}_{\text{out}} = \mathbf{E}_0 + \frac{\varepsilon - 1}{\varepsilon + 2}[3\mathbf{n}(\mathbf{n}\cdot\mathbf{E}_0) - \mathbf{E}_0], \tag{9}$$

where $\mathbf{E}_0$ is the incident laser field, $\mathbf{E}_{\text{out}}$ is the electric field at the sphere surface, $\mathbf{n}$ is a unit vector normal to its surface, and ε is the electric permittivity. Figure 9(a) shows the corresponding dependence of the surface field inhomogeneity on the wavelength for different values of the collision frequency ν. In combination with the experimentally measured linear dependence of the mean ion charge state on the field strength of the laser pulse [see Fig. 9(b)] and Eq. (5) relating ion cutoff to the ion charge, local field enhancement clearly explains the linear wavelength dependence of anisotropy observed in both experiment and simulation. Thus, the dependence of anisotropy on the wavelength is determined by the inhomogeneous surface field around the nanotarget.

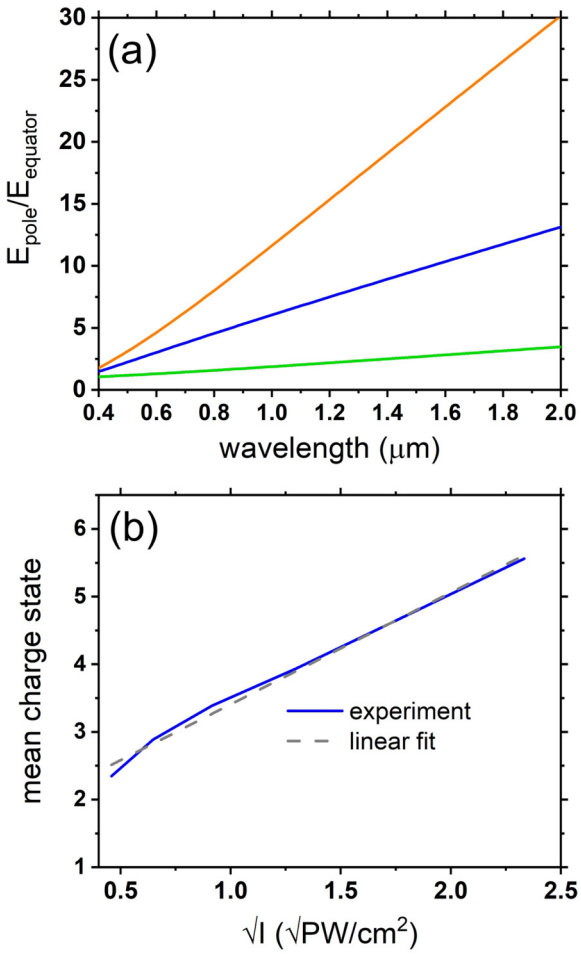

FIG. 9. (a) Electric field enhancement [Eq. (9)] at the surface of a cluster (the estimate is done for the cluster density of $2 \times 10^{22}\text{cm}^{-3}$, corresponding to the density of Ar clusters, and the electron-ion collision frequency of $\nu = 5 \times 10^{15}$ (blue line), following the typical values from previous papers [11,19]); in addition, results for $\nu = 2 \times 10^{15}$ (orange line) and $\nu = 2 \times 10^{16}$ (green line) are shown to demonstrate that the dependence is linear in a broad range of parameters. (b) Measured dependence of the mean ion charge state on the laser field strength. (Experimental conditions: 800 nm wavelength; 60 fs pulse duration; 7 nm Ar cluster size).

However, Eq. (9) and Fig. 9 do not explain the measured dependence of anisotropy on the laser intensity since the field anisotropy is independent of the laser field strength in the first approximation. Nonetheless, the intensity dependence of anisotropy can be explained by MD simulations, which show very good agreement with experiments. In particular, the analysis of the instantaneous plasma temperature distribution indicates another source contributing to ion anisotropy. As can be seen in more detail in Appendix D, plasma temperature is inhomogeneous inside the nanoplasma on the early expansion stages, which is not a big surprise since the electric field creating and heating the plasma is inhomogeneous [Eq. (9) and Fig. 9] and the plasma thermalization does not happen instantaneously. Thus, in addition to the already mentioned anisotropy in the ion charge state and charge density [13], there is plasma temperature anisotropy, both of them grow with laser intensity as shown in Fig. 10, perfectly

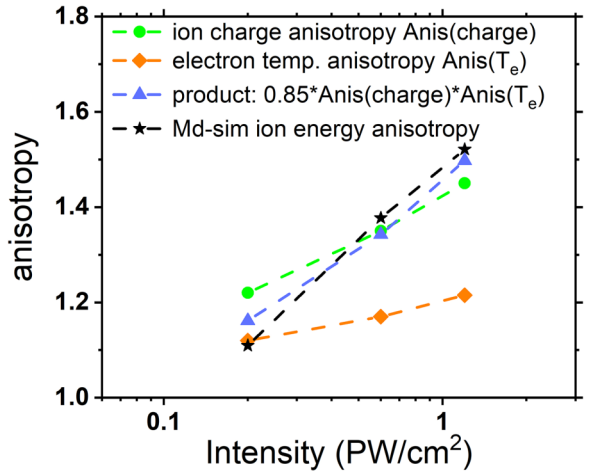

FIG. 10. Parameters contributing to the intensity dependence of the ion anisotropy. (Black stars) MD-simulation results for 1.3 μm pulses [same data set as in Fig. 12(c)]. (Orange rhombuses) The anisotropy of the ion charge state calculated as the ratio of mean ion charge along and orthogonal to the laser polarization. (Green circles) Same but for the electron temperature (defined as the mean electron kinetic energy). (Blue triangles) Product of the previous two contributions.

explaining the trend observed in both experiments and MD simulations.

Another important parameter that can be extracted from the results is the plasma electric permittivity. Using the Drude's expression [Eq. (3)] and Eq. (9), the ratio of electric fields at the pole of the nanosphere (along the laser polarization) with respect to that acting on the equator can be computed by the following, remarkably simple expression:

$$\frac{|\mathbf{E}_{\text{pole}}|}{|\mathbf{E}_{\text{equator}}|} = |\epsilon|, \tag{10}$$

where $\mathbf{E}_{\text{pole}}$ is the electric field at the poles (along the laser polarization) and $\mathbf{E}_{\text{equator}}$ is the electric field at the equator (orthogonal to the laser polarization). Furthermore, assuming over the barrier ionization (OBI) is the dominant mechanism, and that ionization potentials for sequential charge states evolve roughly linearly for outershell electrons, it follows that

$$|\epsilon| \approx \frac{\langle q\rangle_{\text{pole}}}{\langle q\rangle_{\text{equator}}}, \tag{11}$$

where $\langle q\rangle$ is the average ion charge state (see Appendix E for further details). It then follows that the ion anisotropy measurement can be used to evaluate the electric permittivity of spherical nanotargets, and potentially, for more complex nanotargets.

VI. CONCLUSION

In conclusion, our results show that the wavelength dependence of local nanoscale field enhancement in nanospheres can be experimentally traced by the measurement of ion anisotropy in strong-field ionization of nanoclusters. Our results prove that the angular-dependent measurement of ion energy distribution (in the presented case, averaged energy and 0 vs 90 degrees energy anisotropy) provides access to both macroscopic (averaged over the nanostructure) and local nanoscale nanocluster parameters. Ion anisotropy is determined by the local nanoscale field enhancement, while the ion cutoff (as well as average) energy is determined by inverse bremsstrahlung, which follows macroscopic, cycle-averages parameters of the nanoplasma and the optical pulse. The performed scans of the dependence of ion anisotropy and cutoff on a broad range of accessible experimental parameters enables the derivation of universal scaling laws for both of them [Eqs. (6) and (8)].

The obtained results open new directions in studies of nanotargets by detecting angular-dependent charge particle distribution. They rule out a large number of hypotheses describing the ionization of nanoclusters and provide a comprehensive explanation and universal scaling laws, which are supported by experimental results, molecular dynamics simulations, and simplified models. The obtained universal scaling laws should facilitate the development of diagnostics tools and sensors related to the measurement of nanotarget size, electric permittivity, and polarizability [5].

The data that support the findings of this study are available from the corresponding author upon reasonable request.

ACKNOWLEDGMENTS

The work was supported by U.S. Air Force Office of Scientific Research under Awards No. FA-9550-15-1-0037 and No. FA-9550-21-10415. V.L. acknowledges partial support from the NSF RI-1 NeXUS Grant No. 1935885. The authors thank Li Fang, Zhou Wang, and Hyunwook Park for useful discussions.

APPENDIX A: DEPENDENCE OF THE AVERAGED ION CHARGE ON THE CLUSTER DIAMETER

Figure 11 presents the dependence of the averaged ion charge state and the ratio between the ion cutoff and the charge state. These results are in full agreement with the expected scaling of the ion kinetic energy in a thermalized plasma at the end of its expansion [25], see Eq. (5).

APPENDIX B: ANISOTROPY DEPENDENCE ON THE OPTICAL PULSE DURATION

As presented in Fig. 12, ion anisotropy has almost no dependence on the pulse duration at fixed fluence and only depends on the pulse intensity in both both experimental and simulations results.

APPENDIX C: WAVELENGTH DEPENDENCE OF THE INVERSE BREMMSTRAHLUNG HEATING RATE

As noted in the main text, the IBS heating rate, when expressed in terms of the number of cycles [Eq. (4)], all dependence on the wavelength can be gathered in the scaled rate $\bar{\sigma}$, which we define as

$$\bar{\sigma} = \frac{\text{Im}[\varepsilon]}{|\varepsilon + 2|^2}. \tag{C1}$$

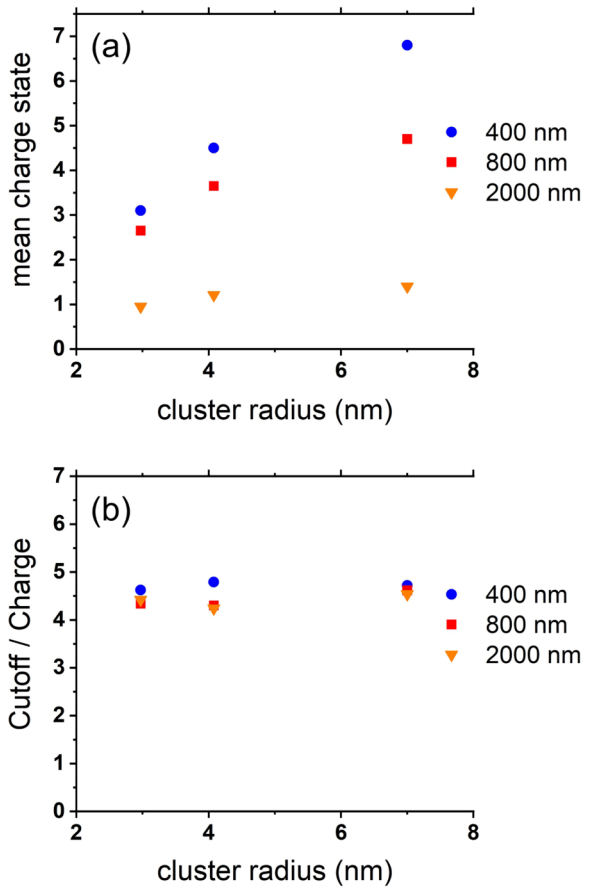

FIG. 11. (a) Measured averaged ion charge state as a function of the cluster radius. (b) Ratio between the ion cutoff shown in Fig. 5(a) and the charge state in (a). The almost perfectly horizontal line proves linear relation between the charge state and the cutoff, as indicated in Eq. (5).

Using the plasma electric permittivity from the Drude model, the scaled rate can be written as follows:

$$\bar{\sigma} = \frac{\omega_p^2 \omega \nu}{\omega_p^2(\omega_p^2 - 6\omega^2) + 9\omega^2(\omega^2 + \nu^2)}. \tag{C2}$$

Clearly, the scaled rate is a function of both the driving wavelength ω, the time-dependent plasma frequency ω_p, and the collision rate ν, such that finding a universal stable behavior appears complicated. This is further exacerbated as the collision frequency ν, despite its fundamental importance, is a majorly unknown quantity with multiple dependencies, ranging from the ionic charge state to the electronic temperature. However, some insight is gained if we introduce the reduced plasma frequency $\bar{\omega}_p = \omega_p/\omega$ and reduced collision frequency $\bar{\nu} = \nu/\omega$, allowing us to write the scaled rate as

$$\bar{\sigma} = \frac{\bar{\omega}_p^2 \bar{\nu}}{\bar{\omega}_p^4 - 6\bar{\omega}_p^2 + 9(1 + \bar{\nu}^2)}. \tag{C3}$$

By inspecting Eq. (C3) it can be concluded that in order for $\bar{\sigma}$ to slowly evolve over a wide range of frequencies (in particular when $\omega_p \gg \omega$, i.e., $\bar{\omega}_p \gg 1$), it is required that $\bar{\nu}$ closely behaves as a second degree polynomial of $\bar{\omega}_p$. This, in turn, implies that, at least on the leading order, $\nu = k\omega_p^2/\omega = kn/\omega$. While such a simple expression might be surprising, it intuitively reflects the fact that the probability of the electron interacting with an ion is proportional to an effective interaction volume covered by the electron on each cycle.

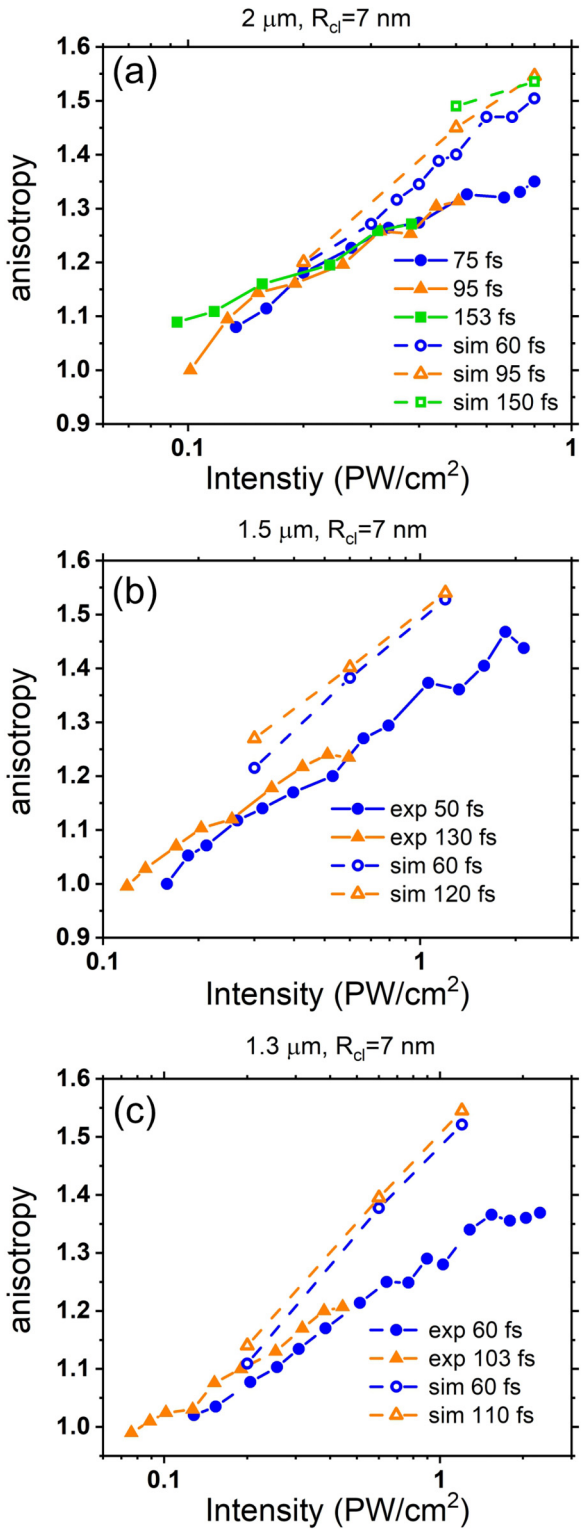

FIG. 12. Dependence of the anisotropy on the pulse duration for (a) 2 μm, (b) 1.5 μm and (c), 1.3 μm. The results in (a) also include MD simulations.

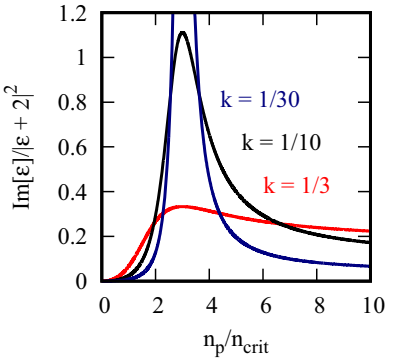

FIG. 13. Scaled heating rate $\bar{\sigma}$ as a function of the relative density for different values of the proportionality factor k. The scaled rate converges rapidly to its asymptotic value for red detuned frequencies.

Therefore, the collisional frequency has to be proportional to the ionic density and its oscillation amplitude or dipole moment (which is implied to scale inversely with ω). Figure 13 shows the scaled heating rate as a function of $\bar{\omega}_p$ or different values of the proportionality factor k. The asymptotic value for red-detuned pulses (large $n_p/n_{\rm crit}$) is quickly reached and reads

$$\bar{\sigma}_{\bar{\omega}_p\to\infty} = \frac{k}{1+9k^2}, \tag{C4}$$

achieving a maximum value of $\bar{\sigma}^{\rm max}_{\bar{\omega}_p\to\infty} = 1/6$ for $k = 1/3$.

APPENDIX D: CHARGE-STATE-RESOLVED MEASUREMENTS

As mentioned in the discussion of Fig. 3 the change in the slope of the dependence of the ion cutoff on the optical pulse intensity is attributed to reaching ionization of the second electron shell of argon (which is equivalent to appearing of ion charges of 9+ and higher). That statement is based on the charge-state-resolved experimental results. Charge state resolution is enabled by applying an accelerating potential to the interaction region, which is done by applying voltage to field plates surrounding the interaction region. It is essentially equivalent to performing a mass-spectrum experiment. An example of the charge-resolved experimental data is shown in Fig. 14(a). The information obtained from this data on the maximum detected ion charge state is presented in Fig. 14(b). It presents the same data on the cutoff as in Fig. 3(b) with the addition of the charge state information.

APPENDIX E: EVIDENCE OF RESONANCE LASER-PLASMA INTERACTION FOR LONG PULSES AT 800 nm

As mentioned in the discussion of Fig. 4, the deviation in the scaling for longer pulses at 800 nm should be caused by approaching the intrapulse plasma resonance conditions. The hypothesis is supported by the experimental results presented in Fig. 15. Figure 15(a) presents an ion spectra from our previous paper [14] at the resonance pump-probe delay when the second pulse interacts with the plasma at resonance density (which enhances the plasma absorption). There is a

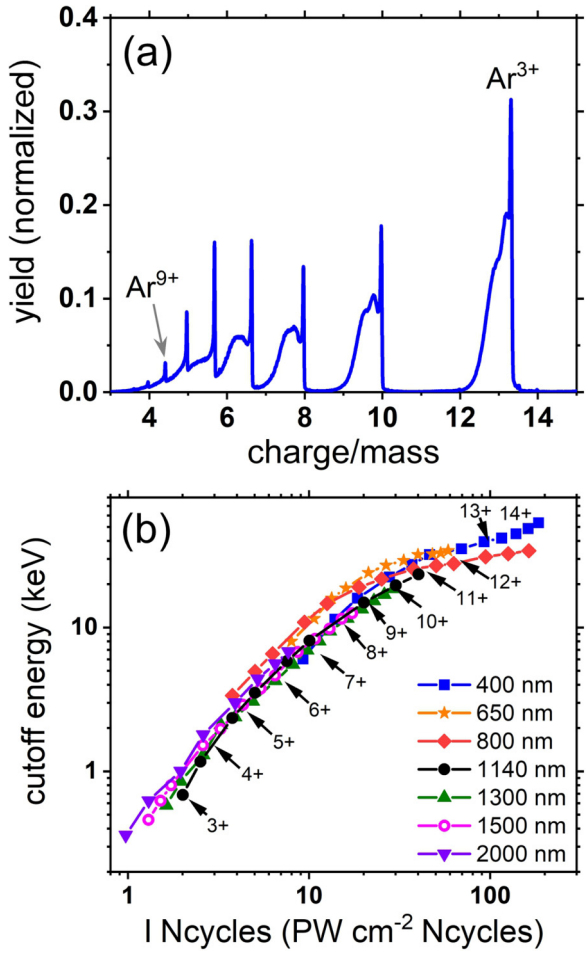

FIG. 14. (a) Example of charge resolved spectra (800 nm, 60 fs, 0.4 PW/cm^2, 7-nm cluster size, along the laser polarization, 2000-V acceleration potential). (b) Charge-resolved cutoff.

clear modification of the shape of the ion spectrum. In the resonance case there is a long plateau with a sharp roll off close to the cutoff, while the ion yield has no pronounced plateau but drops exponentially up to the cutoff in the non-resonant single-pulse ionization case. The results from this

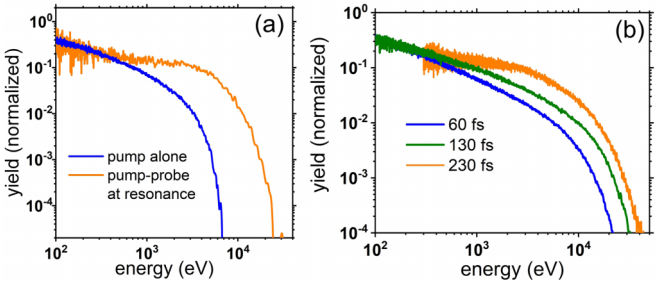

FIG. 15. (a) Example of spectra for pump alone and a resonance pump-probe spectra from [14] (pump: 800 nm, 60 fs, 0.25 PW/cm^2; probe: 1200 nm, 60 fs, 0.1 PW/cm^2; 7-nm Ar cluster size, spectrum is measured along the laser polarization). (b) Examples of ion spectra (along the laser polarization) for fixed fluence of 50 J/cm^2 but varied pulse duration. Pulse parameters: 800 nm, 0.8 PW/cm^2 at 60-fs duration.

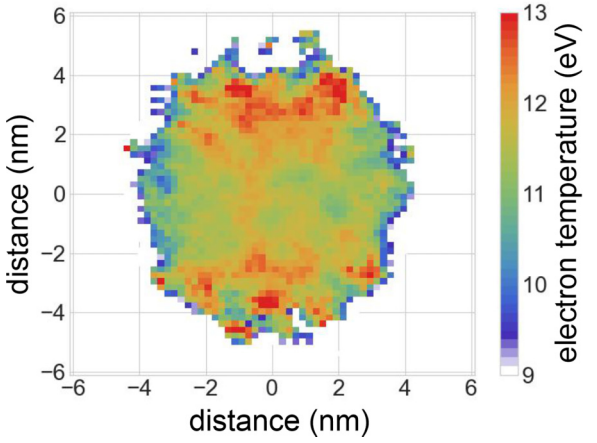

FIG. 16. Example of the (cycle-everaged) electron temperature distribution in the plasmonic nanosphere (laser-ionized nanocluster) calculated in MD simulations. The color represents temperature in eV (locally averaged over the area with 0.4-nm radius). The projection of the slice through the center of the nanosphere is shown, with the laser polarization oriented vertically. Simulation parameters: 1.3 μm wavelegnth, 0.6 PW/cm^2 pulse intensity, 60 fs pulse duration. The presented snapshot is taken at 30 fs after the peak on the pulse.

paper in Fig. 15(b) show a very similar trend. At 60-fs pulse duration, the ion energy distribution has no plateau similar to the single pulse case in Fig. 15(a). However, at longer pulse duration, the spectrum in Fig. 15(b) develops a plateau, and the shape of the ion spectrum clearly resembles the resonance case in Fig. 15(a). It is a clear indicator of intrapulse resonance for longer pulses and shorter wavelengths when the universal scaling of the cutoff is not strictly valid anymore.

APPENDIX F: ANISOTROPY OF ELECTRON TEMPERATURE

As explained in the discussion section, the dependence of the anisotropy on the intensity of optical pulses is governed by the the plasma temperature anisotropy (which, in turn, causes the charge state anisotropy discussed in [13]). Figure 16 presents an example of the electron temperature distribution in a spherical nanoplasma obtained in MD simulations.

APPENDIX G: ANISOTROPY OF ELECTRIC FIELD ENHANCEMENT

Figure 17 shows instantaneous electric field electric field around the cluster and demonstrates the field enhancement at the poles of the nanosphere by the factor of about 6, which is in almost perfect agreement with the analytically predicted value for a 1.3 μm optical pulse (Fig. 17). The result also agrees with previous studies, e.g., [19].

APPENDIX H: ELECTRIC FIELD STRENGTH, ION CHARGE STATE INHOMOGENEITY, AND ELECTRIC PERMITTIVITY

The dipole response of the system has been shown to be responsible for the creation of preferential sites for ionization to take place. This is due to the local field enhancement

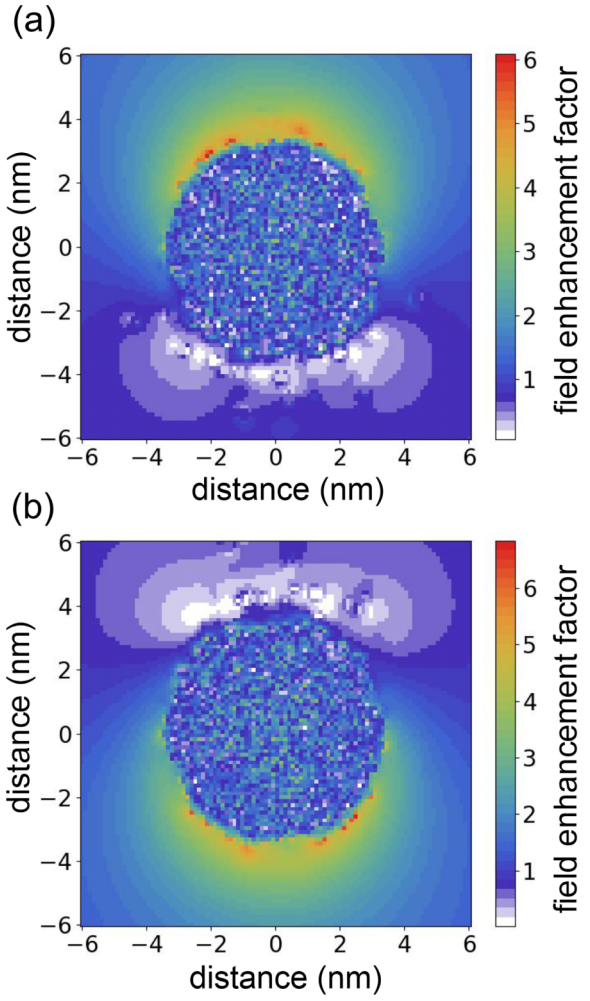

FIG. 17. Amplitude of instantaneous electric field in MD simulations normalized to the field of the laser pulse. The projection of the slice through the center of the nanosphere is shown, with the laser polarization oriented vertically. Simulation parameters: 1.3 μm wavelegnth, 0.6 PW/cm^2 pulse intensity, 60-fs pulse duration. The presented snapshot is taken at (a) the peak on the pulse and (b) half of the optical period later.

and suppression that said dipole field exerts at different regions of the cluster surface. As our study spans a wide range of parameters, the dipole response of both the neutral system and the evolving nanoplasma and its dependence with respect to wavelength and plasma density become relevant. Using Rayleigh's approximation [Eq. (9)] we can compute the electric field at the pole and at the equator as follows:

$$\mathbf{E}_{\text{pole}} = \mathbf{E}_0 + 2\frac{\varepsilon - 1}{\varepsilon + 2}\mathbf{E}_0, \tag{H1}$$

$$\mathbf{E}_{\text{equator}} = \frac{3}{\varepsilon + 2}\mathbf{E}_0, \tag{H2}$$

where the later also corresponds to the homogeneous field inside the cluster. These two fields being collinear, the ratio

of their strengths is readily computed as

$$\frac{\mathbf{E}_{\text{pole}}}{\mathbf{E}_{\text{equator}}} = \frac{1+2\frac{\varepsilon-1}{\varepsilon+2}}{\frac{3}{\varepsilon+2}} = \epsilon. \tag{H3}$$

It should be noted that, as ε is complex, in general these two fields are not in phase. Knowing the field strengths we can proceed to estimate its impact on ionization and surface ionic states. Assuming over the barrier ionization (OBI) is the dominant ionization mechanism, the critical field (that removes the potential barrier) is

$$E_c(q) = \frac{\left(I_p^q\right)^2}{4q}, \tag{H4}$$

where I_p^q is the ionization potential for an ion with charge q. Naturally, it follows that the sequential removal of electrons requires increasingly higher field strengths, which is reflected on increasing values of their ionization potentials. While the ionization energy can evolve in a complex manner, it can be approximated to be linear with respect to the ionic charge $I_p^q = qI_p^1$ (with I_p^1 being the ionization potential of the neutral atom) for electrons in the valence shell. Therefore, the critical electric field is approximately

$$E_c(q) \approx q\frac{\left(I_p^1\right)^2}{4}. \tag{H5}$$

This result allows us to estimate the charge state along the cluster surface, and along Eq. (H3) we obtain

$$|\epsilon| \approx \frac{\langle q\rangle_{\text{pole}}}{\langle q\rangle_{\text{equator}}}. \tag{H6}$$

Therefore, the wavelength dependence of the anisotropy can be understood, at least partially (see Appendix D), as a consequence of different ionic charge states induced by the frequency-dependent electric permittivity of the system.

[1] V. Kuncser and L. Miu, *Size Effects in Nanostructures: Basics and Applications*, Springer Series in Materials Science (Springer, Berlin, 2014).

[2] T. Fennel, K.-H. Meiwes-Broer, J. Tiggesbäumker, P.-G. Reinhard, P. M. Dinh, and E. Suraud, Laser-driven nonlinear cluster dynamics, Rev. Mod. Phys. **82**, 1793 (2010).

[3] L. Seiffert, S. Zherebtsov, M. F. Kling, and T. Fennel, Strong-field physics with nanospheres, Adv. Phys.: X **7**, 2010595 (2022).

[4] K. A. Altammar, A review on nanoparticles: Characteristics, synthesis, applications, and challenges, Front. Microbiol. **14**, 1155622 (2023).

[5] H. Nasrollahpour, B. J. Sánchez, M. Sillanpää, and R. Moradi, Metal nanoclusters in point-of-care sensing and biosensing applications, ACS Appl. Nano Mater. **6**, 12609 (2023).

[6] K. K. Ostrikov, F. Beg, and A. Ng, *Colloquium*: Nanoplasmas generated by intense radiation, Rev. Mod. Phys. **88**, 011001 (2016).

[7] E. Saydanzad, J. Li, and U. Thumm, Strong-field ionization of plasmonic nanoparticles, Phys. Rev. A **106**, 033103 (2022).

[8] U. Saalmann, C. Siedschlag, and J. M. Rost, Mechanisms of cluster ionization in strong laser pulses, J. Phys. B: At. Mol. Opt. Phys. **39**, R39 (2006).

[9] Y. Fukuda, Y. Akahane, M. Aoyama, N. Inoue, H. Ueda, Y. Kishimoto, K. Yamakawa, A. Faenov, A. Magunov, T. Pikuz *et al.*, Generation of X rays and energetic ions from superintense laser irradiation of micron-sized ar clusters, Laser Part. Beams **22**, 215 (2004).

[10] E. Lamour, C. Prigent, J. P. Rozet, and D. Vernhet, X-ray production in short laser pulse interaction with rare gas clusters, J. Phys.: Conf. Ser. **88**, 012035 (2007).

[11] T. Ditmire, T. Donnelly, A. M. Rubenchik, R. W. Falcone, and M. D. Perry, Interaction of intense laser pulses with atomic clusters, Phys. Rev. A **53**, 3379 (1996).

[12] V. Krainov and M. Smirnov, Cluster beams in the super-intense femtosecond laser pulse, Phys. Rep. **370**, 237 (2002).

[13] H. Park, A. Camacho Garibay, Z. Wang, T. Gorman, P. Agostini, and L. F. DiMauro, Unveiling the inhomogeneous nature of strong field ionization in extended systems, Phys. Rev. Lett. **129**, 203202 (2022).

[14] V. Leshchenko, B. Smith, A. Camacho Garibay, P. Agostini, L. Fang, and L. F. DiMauro, Nanoplasma resonance condition in the middle-infrared spectral range, Phys. Rev. E **107**, 055207 (2023).

[15] U. Even, Pulsed supersonic beams from high pressure source: Simulation results and experimental measurements, Adv. Chem. **2014**, 636042 (2014).

[16] B. van de Waal, G. Torchet, and M.-F. de Feraudy, Structure of large argon clusters Ar_N, $10^3 < N < 10^5$: Experiments and simulations, Chem. Phys. Lett. **331**, 57 (2000).

[17] T. Gorkhover, S. Schorb, R. Coffee, M. Adolph, L. Foucar, D. Rupp, A. Aquila, J. D. Bozek, S. W. Epp, B. Erk, L. Gumprecht, L. Holmegaard, A. Hartmann, R. Hartmann, G. Hauser, P. Holl, A. Hömke, P. Johnsson, N. Kimmel, K.-U. Kühnel *et al.*, Femtosecond and nanometre visualization of structural dynamics in superheated nanoparticles, Nat. Photonics **10**, 93 (2016).

[18] Y. Fukuda, K. Yamakawa, Y. Akahane, M. Aoyama, N. Inoue, H. Ueda, and Y. Kishimoto, Optimized energetic particle emissions from Xe clusters in intense laser fields, Phys. Rev. A **67**, 061201(R) (2003).

[19] C. Prigent, C. Deiss, E. Lamour, J.-P. Rozet, D. Vernhet, and J. Burgdörfer, Effect of pulse duration on the x-ray emission from ar clusters in intense laser fields, Phys. Rev. A **78**, 053201 (2008).

[20] J. Zweiback, T. Ditmire, and M. D. Perry, Femtosecond time-resolved studies of the dynamics of noble-gas cluster explosions, Phys. Rev. A **59**, R3166 (1999).

[21] T. Ditmire, E. Springate, J. W. G. Tisch, Y. L. Shao, M. B. Mason, N. Hay, J. P. Marangos, and M. H. R. Hutchinson, Explosion of atomic clusters heated by high-intensity femtosecond laser pulses, Phys. Rev. A **57**, 369 (1998).

[22] Z. Wang, A. Camacho Garibay, H. Park, U. Saalmann, P. Agostini, J. M. Rost, and L. F. DiMauro, Universal high-energy photoelectron emission from nanoclusters beyond the atomic limit, Phys. Rev. Lett. **124**, 173201 (2020).

[23] K. Nishihara, H. Amitani, M. Murakami, S. Bulanov, and T. Esirkepov, High energy ions generated by laser driven coulomb explosion of cluster, Nucl. Instrum. Methods Phys. Res. Sect. A **464**, 98 (2001), Proceedings of the 13th International Symposium on Heavy Ion Intertial Fusion.

[24] Y. Tao, R. Hagmeijer, E. T. A. van der Weide, H. M. J. Bastiaens, and K.-J. Boller, Revisiting argon cluster formation in a planar gas jet for high-intensity laser matter interaction, J. Appl. Phys. **119**, 164901 (2016).

[25] W. Demtroder and W. Jantz, Investigation of laser-produced plasmas from metal-surfaces, Plasma Phys. **12**, 691 (1970).

[26] E. Skopalová, Y. C. El-Taha, A. Zaïr, M. Hohenberger, E. Springate, J. W. G. Tisch, R. A. Smith, and J. P. Marangos, Pulse-length dependence of the anisotropy of laser-driven cluster explosions: Transition to the impulsive regime for pulses approaching the few-cycle limit, Phys. Rev. Lett. **104**, 203401 (2010).

[27] V. Kumarappan, M. Krishnamurthy, and D. Mathur, Asymmetric high-energy ion emission from argon clusters in intense laser fields, Phys. Rev. Lett. **87**, 085005 (2001).

[28] J. W. G. Tisch, Clusters in intense laser fields, in *Atoms, Solids, and Plasmas in Super-Intense Laser Fields*, edited by D. Batani, C. J. Joachain, S. Martellucci, and A. N. Chester (Springer, Boston, 2001), pp. 99–118.

[29] C. Jungreuthmayer, M. Geissler, J. Zanghellini, and T. Brabec, Microscopic analysis of large-cluster explosion in intense laser fields, Phys. Rev. Lett. **92**, 133401 (2004).

[30] D. Mathur and F. A. Rajgara, Communication: Ionization and Coulomb explosion of xenon clusters by intense, few-cycle laser pulses, J. Chem. Phys. **133**, 061101 (2010).

[31] H. J. W. Strutt, LVIII. on the scattering of light by small particles, The London, Edinburgh, and Dublin Philosophical Magazine and Journal of Science **41**, 447 (1871).

[32] J. D. Jackson, *Classical Electrodynamics*, 3rd ed. (Wiley, New York, 1999).